Supporting Information

Solid-Solid Phase Transformations Induced through Cation Exchange and Strain, in 2D Heterostructured Copper Sulfide Nanocrystals

Don-Hyung Ha[a], Andrew H. Caldwell[a], Matthew J. Ward[b], Shreyas Honrao[a], Kiran Mathew[a], Robert Hovden[c], Margaret K.A. Koker[b], David A. Muller[c,d], Richard G. Hennig[a], and Richard D. Robinson[,a]*

Cornell University, Ithaca, New York 14853, United States
[a]Department of Materials Science and Engineering
[b]Cornell High Energy Synchrotron Source (CHESS)
[c]School of Applied and Engineering Physics
[d]Kavli Institute at Cornell for Nanoscale Science, Ithaca, New York 14853, United States

* To whom correspondence should be addressed. E-mail: rdr82@cornell.edu,

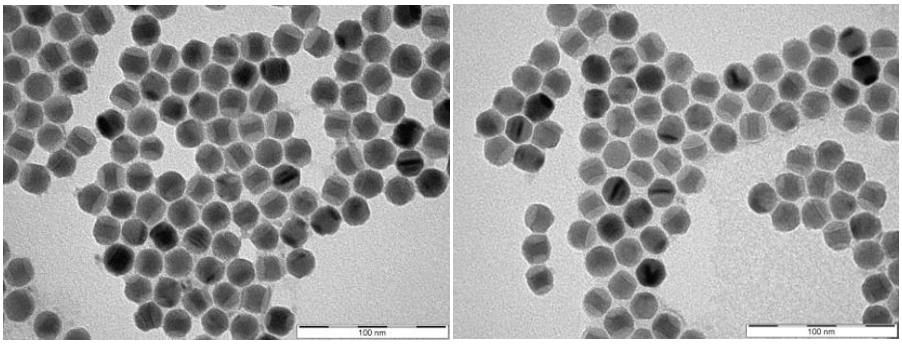

Figure S1. TEM images of as-synthesized heterostructured NCs (left) and of the same sample after one week (right). Heterostructured NCs (left) retain their interface structure even after one week of air exposure in a vial (right). Dried NCs are stored in a vial after cation exchange and kept in air for a week. NCs are then re-dispersed in hexane for TEM imaging.

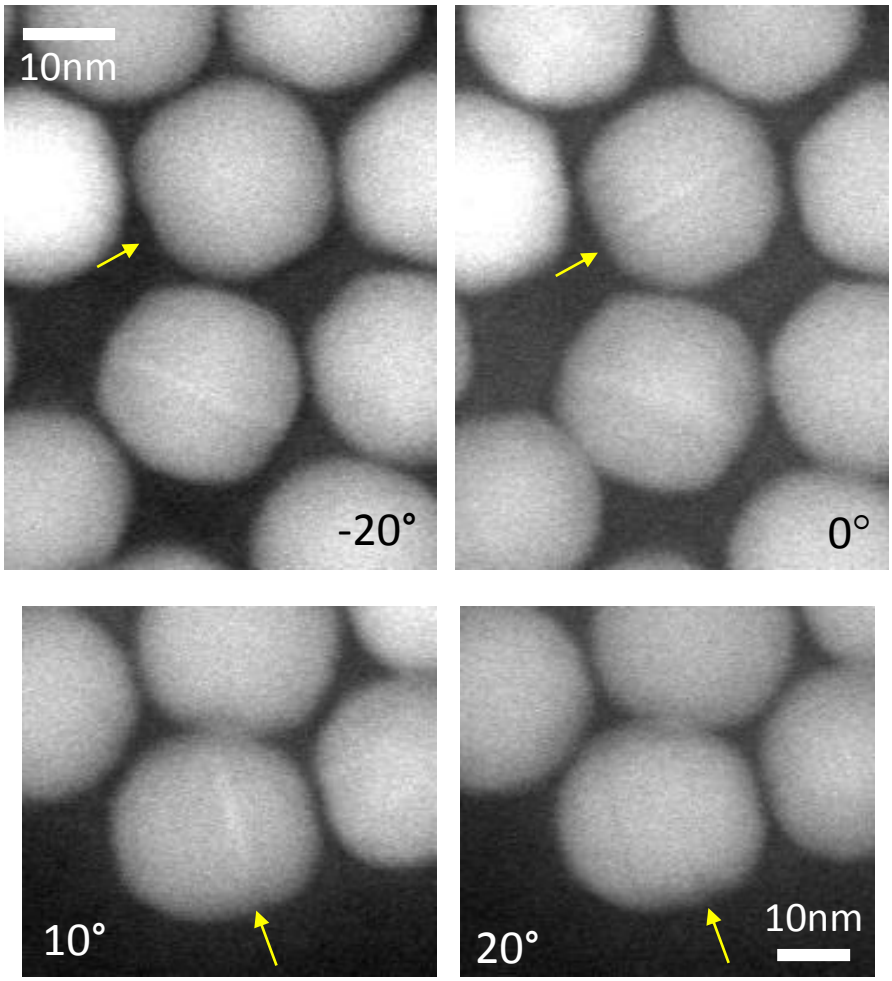

Figure S2. HAADF-STEM images for the final sample (Cu-S/ZnS, Fig. 1e). Only copper layers oriented parallel or near-parallel to the electron beam will be clearly visible. The lack of a visible copper layers, does not imply that a layer is not present. When the specimen is tilted relative to the beam direction, copper layers appear and disappear.

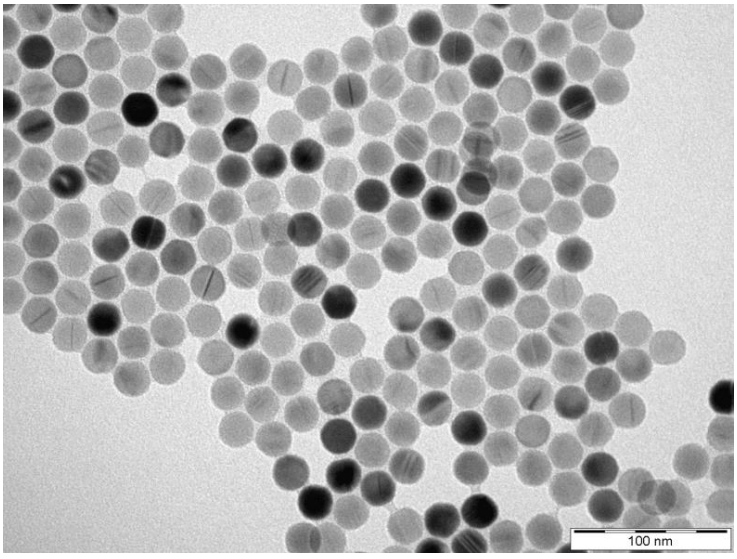

Supplementary Figure 3. TEM image of the NCs reacted under an aggressive environment. After roxbyite NCs are reacted for 4 hours at 50 °C, the temperature is increased to 100 °C and kept for 30 minutes. Approximately 30 % of the NCs show a thin layer.

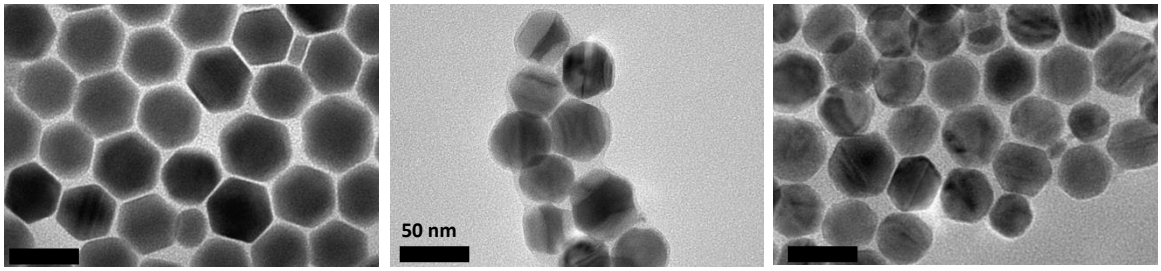

Figure S4. TEM images of ~40 nm sized NCs during cation exchange reaction. Starting roxbyite NCs (left) show ~40 nm size.[1] 7 minutes of reaction with Zn solution leads to heterostructured NCs (center). The final NCs (right) show Moiré pattern and thin layer in the center of the NCs.

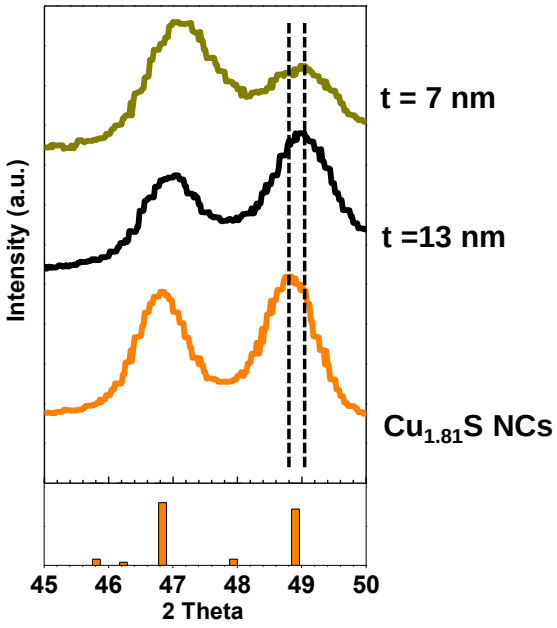

Figure S5. Magnified form of Fig. 3a with vertical lines to clarify the shift to higher angles.

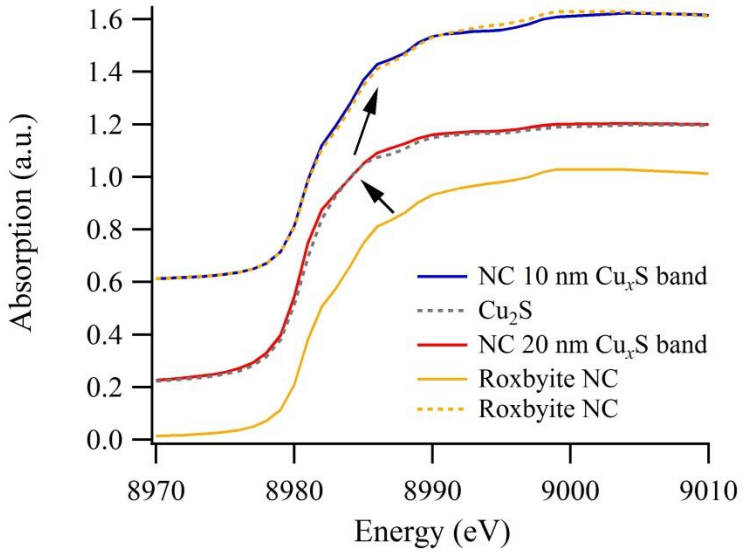

Figure S6. Cu K-edge XANES of roxbyite NCs, Cu_2S, and NC samples with *t* = 20 nm and 15 nm. Shift observed in the copper K-edge XANES from roxbyite phase to Cu_2S phase at the beginning of the chemical transformation, when the thickness of the Cu_xS band, *t*, is 20 nm. XANES shifts back toward the roxbyite phase when $t \leq 10$ nm.

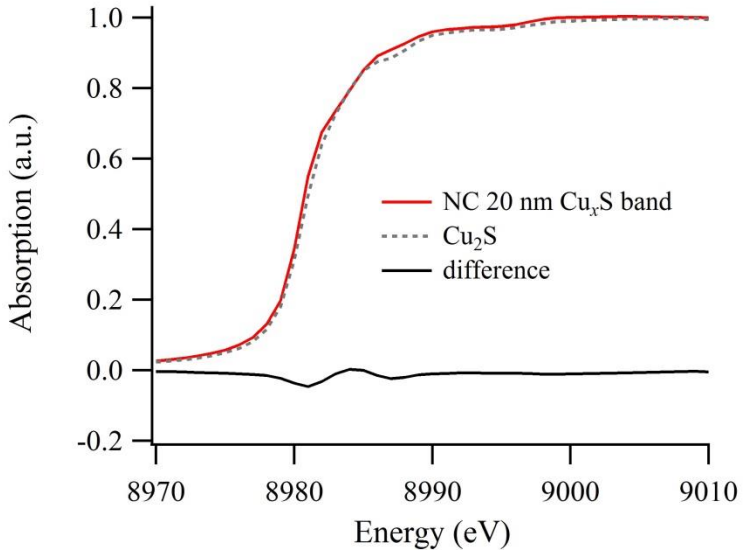

Figure S7. Difference spectrum from Cu K-edge XANES of NC sample with *t* = 20 nm and Cu_2S.

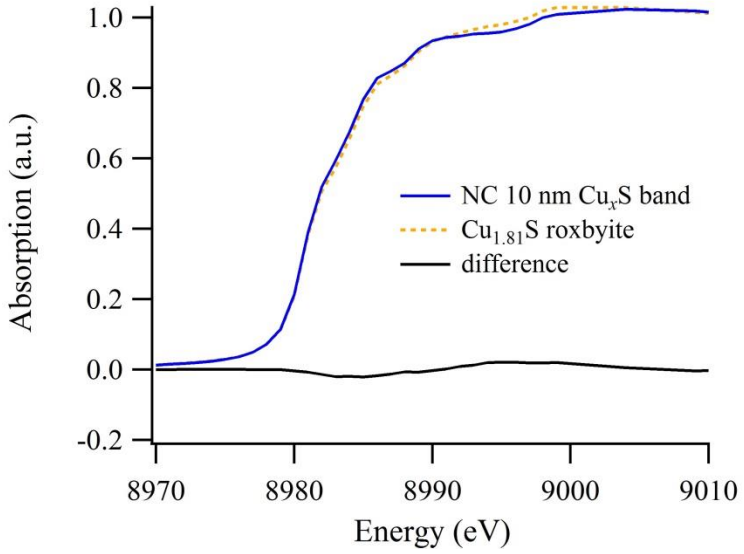

Figure S8. Difference spectrum from Cu K-edge XANES of NC sample with *t* = 10 nm and $Cu_{1.81}S$ roxbyite.

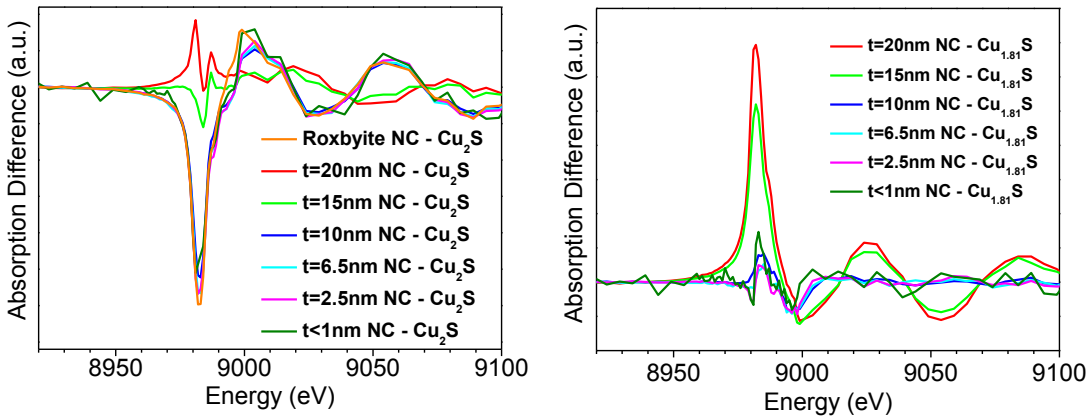

Figure S9. (Left) Absorption difference of XANES spectra taken between NC samples and Cu_2S standard. (Right) Absorption difference of XANES spectra taken between NC samples and roxbyite NC sample.

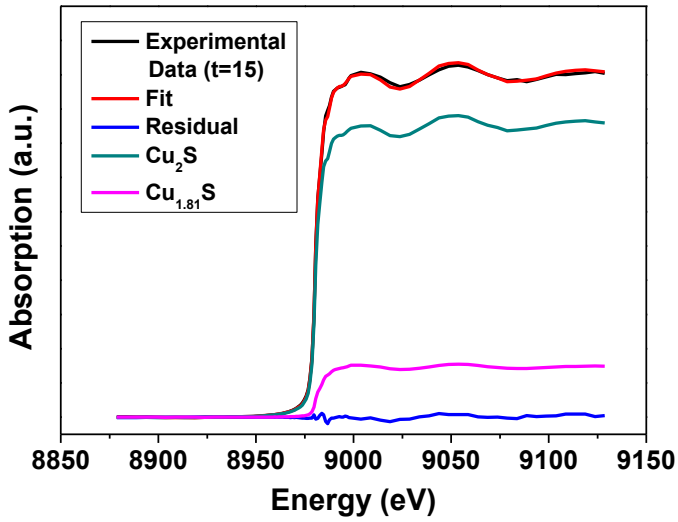

Figure S10. Linear Combination-XANES fit of NC sample with *t* = 15 nm using $Cu_{1.81}S$ (roxbyite) and Cu_2S (djurleite / low chalcocite) as reference standards.

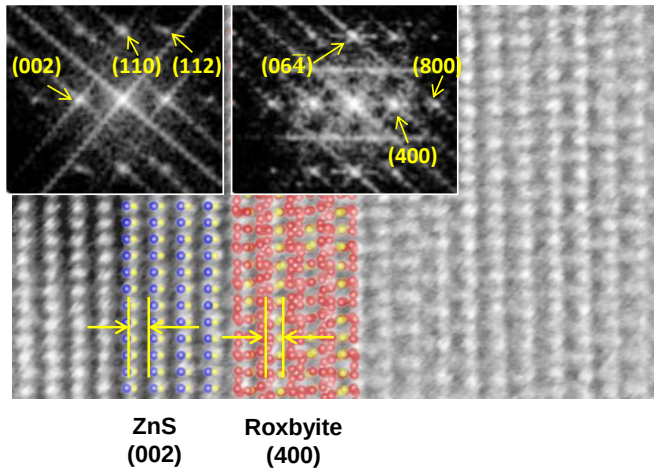

Figure S11. FFT of HRTEM image of ZnS and roxbyite grains from Fig. 5b.

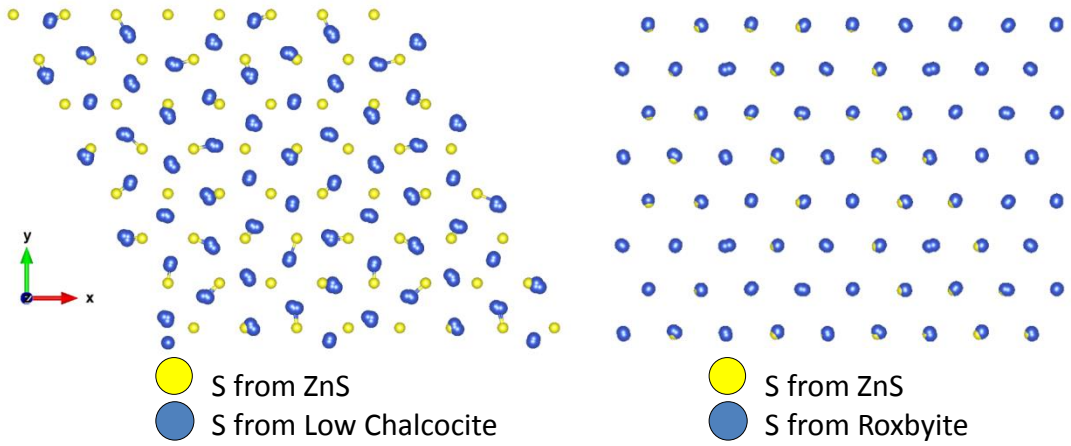

Figure S12. Superimposed sulfur sublattice to the interfacial plane. Sulfur sublattice from low chalcocite and that of ZnS match poorly (left) while sulfur sublattice between roxbyite and ZnS is well aligned (right). Perspective (z-axis) is looking down the <010> of low chalcocite, <100> of roxbyite, and <001> of zinc sulfide lattices.

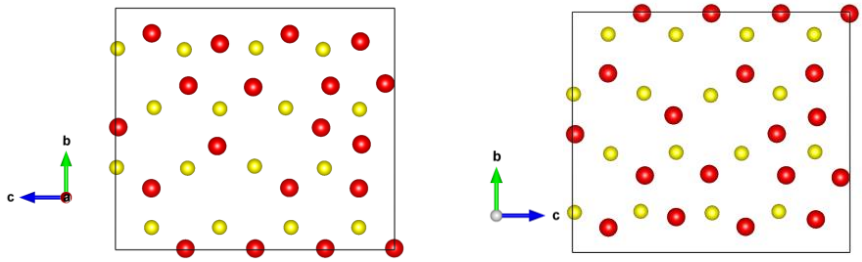

Figure S13. The (100) plane (left) and ($\bar{1}00$) plane (right) of roxbyite phase. They share a very similar atomic arrangement.

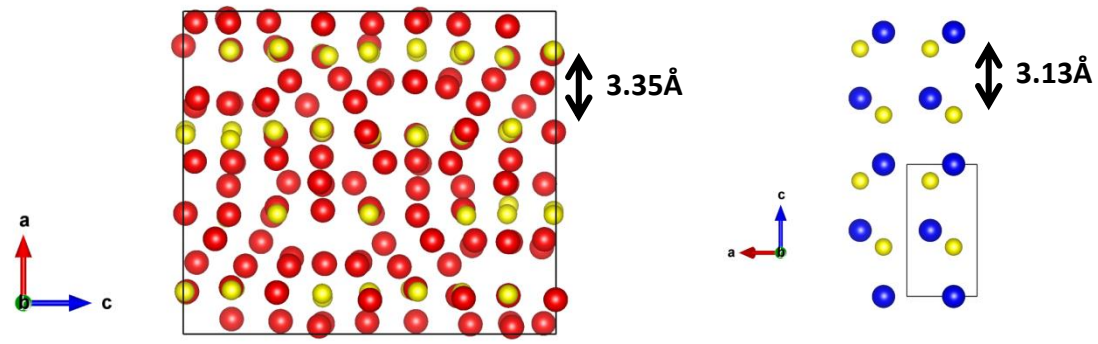

Figure S14. Distances between S-S sub-layers perpendicular to the epitaxial plane of roxbyite (left) and ZnS (right). They show ~8 % different S-S sub-layer distance which is much higher than the lattice mismatch along the epitaxial plane (~1.1%).

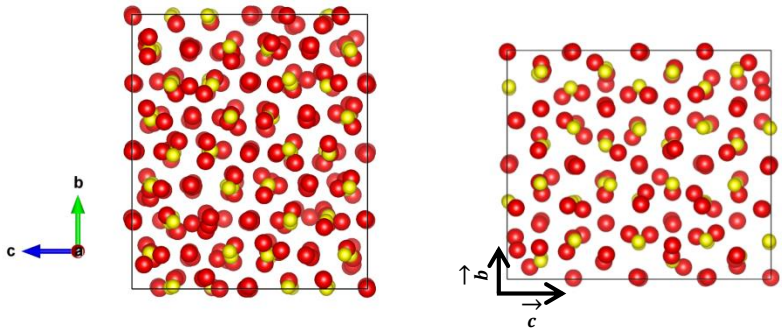

Figure S15. The epitaxial plane for djurleite (left) and roxbyite (right) for ZnS. Djurleite and roxbyite share a similar sulfur sub-lattice (S-S distances for djurleite and roxbyite are 3.91Å and 3.87Å, respectively). However, S-S distance in djurleite has much higher standard deviation than that in roxbyite (0.13 Å for djurleite vs. 0.08 Å for roxbyite).

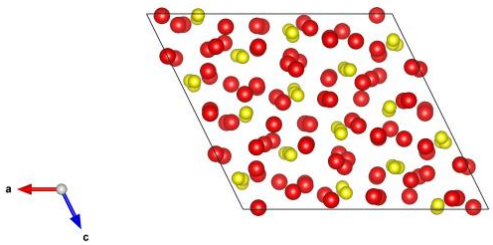

Figure S16. Epitaxial plane for low chalcocite. The epitaxial plane for low chalcocite are poorly matched with hexagonal lattice.

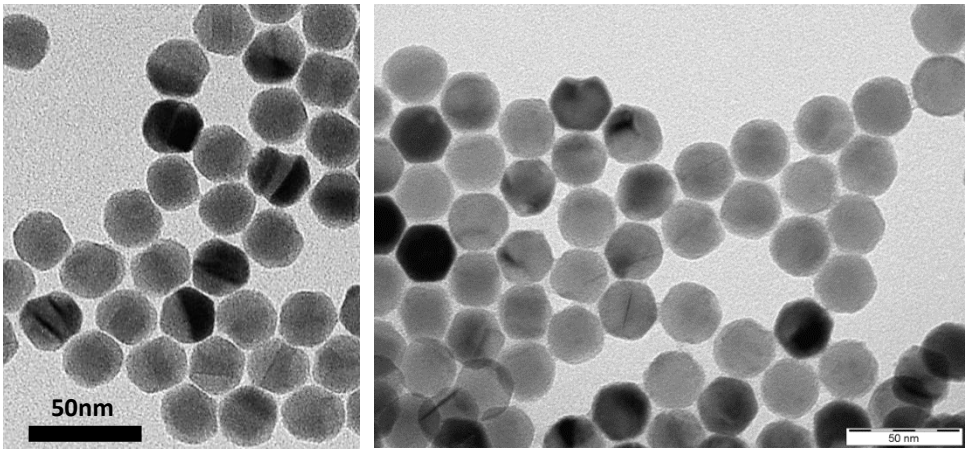

Figure S17. TEM images of NCs reacted for 2 minutes with Cd solution (left) and the final sample (right).

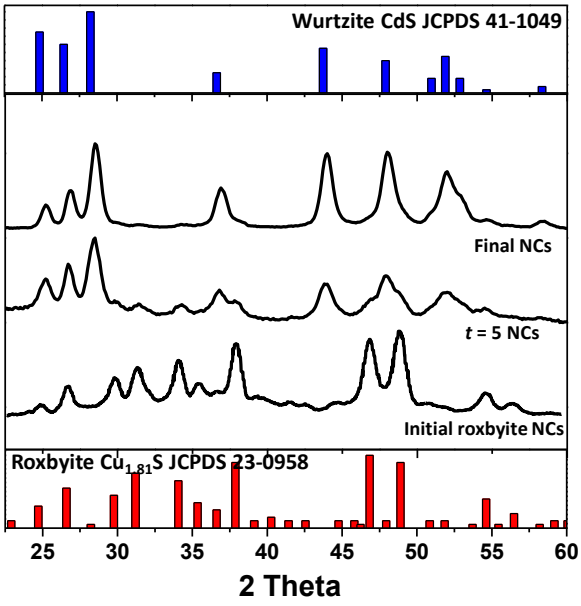

Figure S18. XRD results of samples from copper sulfide to cadmium sulfide

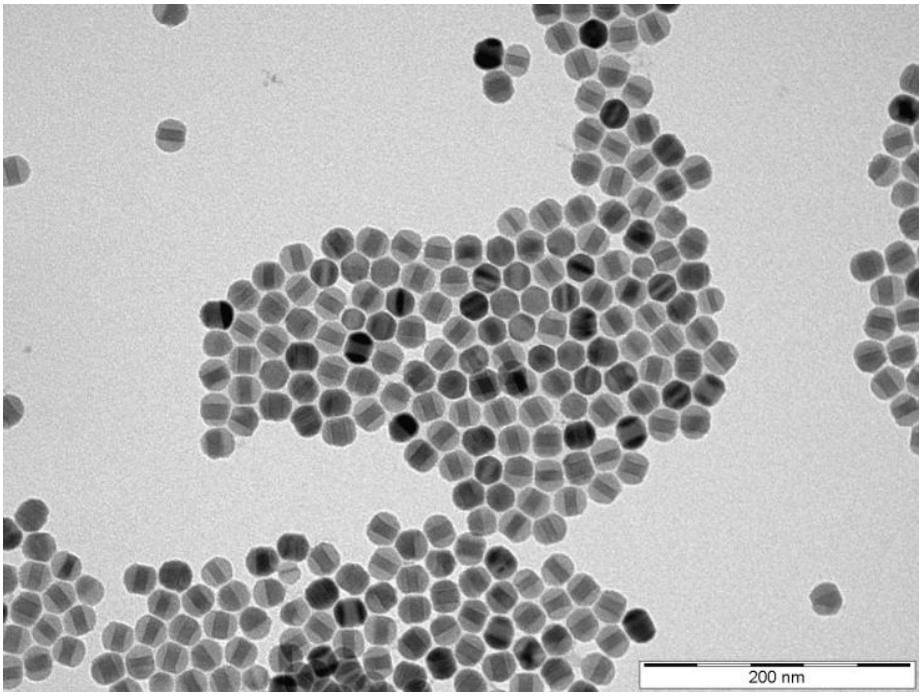

Figure S19. TEM image with low magnification of the heterostructured (Cu-S/ZnS) NC sample (Fig. 1c)

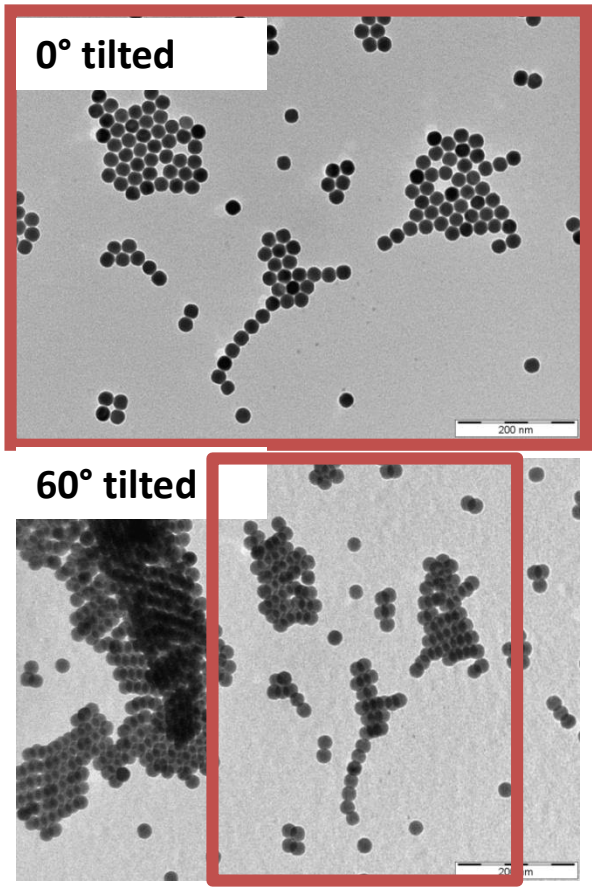

Figure S20. TEM images of roxbyite NCs. 60° tilted TEM image (bottom) confirms that the starting roxbyite NCs are spherical. Red box displays the sample area before and after the TEM stage tilting experiment.

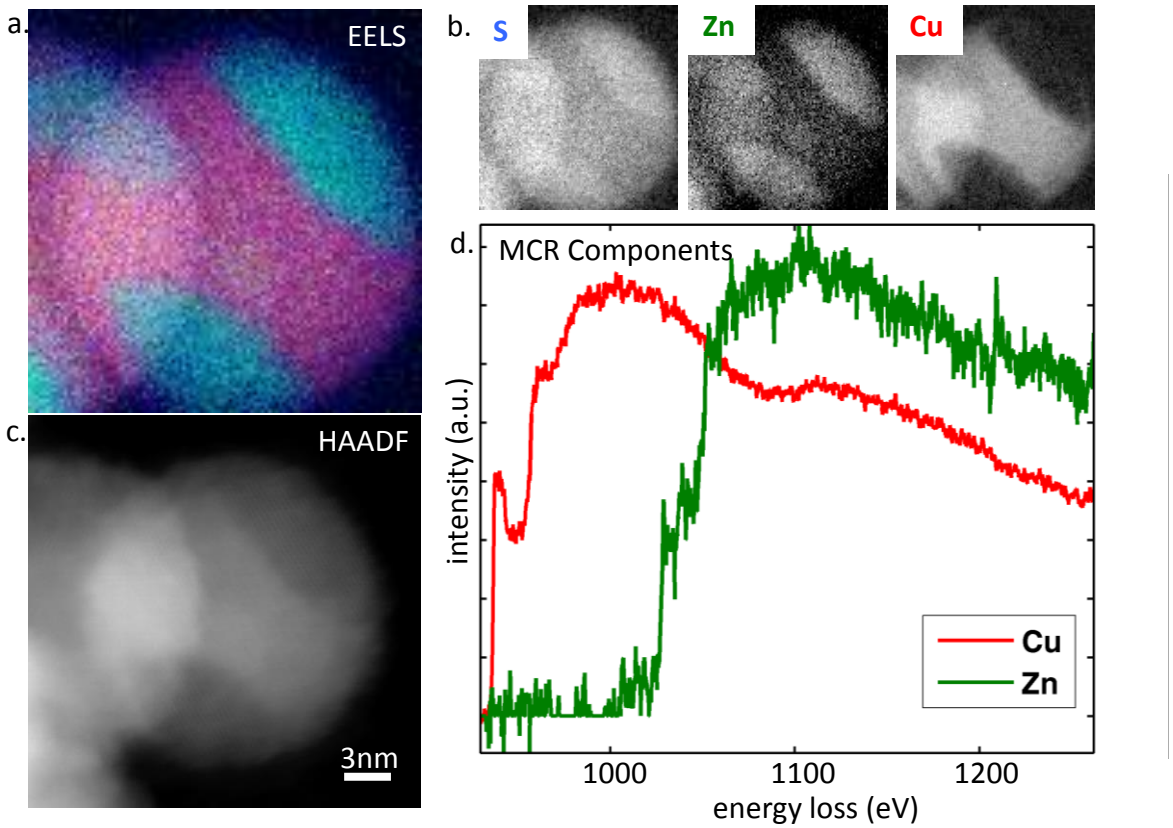

Figure S21. Multivariate curve resolution (MCR) analysis for Cu and Zn EELS map of an intermediate product nanocrystal. a.) RGB composite image made from three chemical maps (b.), S, Zn, and Cu. c.) a HAADF image of the nanoparticle. d.) the MCR spectral components extracted after 20 iterations. MCR allows better estimation of the convoluted Zn and Cu edges.

Table S1. Thickness of copper sulfide layer in heterostructured NCs

Reaction time at 50 °C (minutes)	Copper sulfide layer thickness "*t*" (nm)
5	20 (std. dev. 8%)
15	19 (std. dev. 6%)
30	12 (std. dev. 6%)
75	8 (std. dev. 8%)
150	3 (std. dev. 29%)
240	1.5 (std. dev. 35%)
Final	<1

Table S1 show the thickness of copper sulfide layer in heterostructured NCs as a function of cation exchange reaction time (a diameter of initial copper sulfide NCs is 22 nm)

Table S2. Linear combination fitting results for the heterostructured NC samples

Sample (Copper sulfide layer thickness, *t*)	a_μ ($Cu_{1.81}S$)	b_μ (Cu_2S)
*22 nm	1	0
20 nm	0.03 (±0.05)	0.97 (±0.05)
15 nm	0.15 (±0.03)	0.85 (±0.03)
10 nm	0.74 (±0.04)	0.26 (±0.04)
6 nm	0.80 (±0.05)	0.20 (±0.05)
2.5 nm	0.76 (±0.04)	0.24 (±0.04)
1 nm	0.67 (±0.04)	0.33 (±0.04)
<1 nm	0.47 (±0.12)	0.53 (±0.12)

*roxbyite NC starting material

Table S2 shows the copper K-edge XANES linear combination fitting results as a function of copper sulfide layer thickness in the NC heterostructures during the chemical transformation from roxbyite to zinc sulfide.

Table S3 – Cu K-edge E_0 for the heterostructured NC samples, $Cu_{1.81}S$, and Cu_2S

Sample (Copper sulfide layer thickness, *t*)	E_0 (eV)
20 nm	8980.1 (±0.1)
15 nm	8980.3 (±0.1)
10 nm	8980.4 (±0.1)
6 nm	8980.4 (±0.1)
2.5 nm	8980.5 (±0.1)
1 nm	8980.6 (±0.1)
< 1 nm	8980.5 (±0.1)
$Cu_{1.81}S$	8980.4 (±0.1)
Cu_2S	8980.3 (±0.1)

Table S3 shows the binding energy threshold for the copper K-edge (1s electron) in the heterostructured NC samples, $Cu_{1.81}S$, and Cu_2S. All energies were calibrated using a copper reference foil measured downstream of the sample, the XANES spectra of all samples were aligned on the same energy grid after calibration. The oxidation state of copper in all the heterostructured samples, $Cu_{1.81}S$, and Cu_2S is 1+, as expected.[2]

Table S4 – Zn K-edge E_0 for the heterostructured NC samples, ZnS, and ZnO

Sample (Copper sulfide layer thickness, *t*)	E_0 (eV)
20 nm	9662.3 (±0.1)
15 nm	9661.8 (±0.1)
10 nm	9661.4 (±0.1)
6 nm	9661.2 (±0.1)
2.5 nm	9661.3 (±0.1)
1 nm	9661.2 (±0.1)
< 1 nm	9661.1 (±0.1)
ZnS	9661.0 (±0.1)
ZnO	9661.2 (±0.1)

Table S4 shows the binding energy threshold for the zinc K-edge (1s electron) in heterostructured NC samples, ZnS, and ZnO. All energies were calibrated using a zinc reference foil measured downstream of the sample, the XANES spectra of all samples were aligned on the same energy grid after calibration. The oxidation state of zinc in the heterostructured NCs, ZnS, and ZnO is 2+, as expected. The larger value of E_0 for sample A can be attributed to the superposition of $\mu(E)$ contributions from ZnO and ZnS and is not indicative of a change in oxidation state of Zn.

Table S5. Calculated total strain energy and strain energy density

Copper sulfide layer thickness (*t*)	Total Strain Energy (kBar)	Strain Energy Density ($J \cdot nm^{-3}$)
2.2	0.035	3.5E-21
3.3	0.045	4.5E-21
4.84	0.085	8.5E-21
7.634	0.07	7E-21
12.1	0.045	4.5E-21
16.5	0.02	2E-21
19.8	0.005	0.5E-21

Methods

Synthesis

Chemicals

All synthesis was carried out in a dry, oxygen-free, nitrogen gas atmosphere by employing standard Schlenk line and glove box techniques. Acetone (≥ 99.5%), hexanes (≥ 98.5%), ethanol (≥ 99.5%), toluene (≥ 99.9%), oleylamine (70%), 1-Octadecene (ODE, 90%) tri-*n*-octylphosphine (TOP, 97%), $ZnCl_2$ (99.999%), di-tert-butyl disulfide (97%), and $CdCl_2$ (99.99%) were purchased from Aldrich. $CuCl_2 \cdot 2H_2O$ (99.999%) was purchased from Alfa Aesar.

Roxbyite nanocrystal synthesis

The synthesis of roxbyite nanocrystals (NCs) is slightly modified from the standard procedure.[1] A mixture of $CuCl_2 \cdot 2H_2O$ (340.8 mg) and oleylamine (59 mL) was vacuumed for 30 minutes at room temperature and another 30 minutes at 100 °C to remove water and impurities. The solution was then heated to 200 °C under a nitrogen flow. The solution was maintained at 200 °C for one hour after it becomes transparent yellow color. The di-tert-butyl disulfide solution (8 mL) was injected into the solution at 180 °C and the reaction was allowed to proceed for 40 minutes. The solution was quenched with a water bath and the NCs were collected by centrifugation and washed twice with hexane/acetone. The roxbyite NCs were kept in hexane.

Nanocrystal cation exchange (Copper sulfide to zinc sulfide)

Concentrated Zn ion solution was prepared by dissolving $ZnCl_2$ in oleylamine. A mixture of $ZnCl_2$ (500 mg) and oleylamine (20 mL) was vacuumed at 100 °C for 30 minutes and heated to 180 °C. The solution was kept at 180 °C for 30 minutes under a nitrogen flow. The solution was then kept at 100 °C under nitrogen.

The roxbyite NC solution was prepared by dispersing dry roxbyite NCs (35 mg) in 7 mL of TOP. This solution was kept at room temperature in a glove box for 3 hours before the cation exchange reaction.

A separate flask was prepared for the cation exchange reaction. A mixture of toluene (30 mL) and pre-prepared concentrated Zn solution (9.33 mL) was heated to 50 °C. When the temperature was stabilized, the roxbyite NC/TOP solution was injected into the Zn solution. Aliquots at different reaction times were taken and immediately quenched by injecting into cold acetone. The copper sulfide layer thickness as a function of reaction time is shown in **Table S1**. For the final sample, the solution was heated to 100 °C and kept for 10 minutes to facilitate the reaction.

Nanocrystal cation exchange (Copper sulfide to cadmium sulfide)

A roxbyite NC solution was prepared by dispersing dry roxbyite NCs (5 mg) in 5 mL of TOP. This solution was kept at room temperature in a glove box for 3 hours before the cation exchange reaction.

A mixture of $CdCl_2$ (44.68 mg), ODE (8.75 mL), and oleylamine (8.75 mL) was vacuumed at 100 °C for 30 minutes. Then the solution was cooled down to 50 °C. When the temperature was stable, the roxbyite NC/TOP solution was injected into the Cd solution. The aliquots at different reaction times were taken and immediately quenched by injecting into cold acetone. The cation exchange reaction with Cd is much faster than that with Zn. 2 minutes of the reaction results in a copper sulfide layer thickness of 5 nm (**Fig. S17**). The reaction was completed in 30 minutes (final sample). XRD results show that NCs are fully converted to wurtzite CdS (**Fig. S18**). Fast kinetics of the cation exchange reaction between copper sulfide and Cd and the large interfacial strains (~6.8 %) between copper sulfide and CdS result in a less-controlled morphology than that produced by the transformation from copper sulfide to ZnS (**Fig. S17**). The cation exchange reaction from copper sulfide to CdS occurs in 20 minutes while that to ZnS takes five hours at 50 °C. Additionally, the Cu to Cd ion ratio for the cation reaction is much lower than the Cu to Zn ratio (Cu:Cd≈1:4 vs. Cu:Zn≈1:20).

Transmission Electron Microscopy

TEM images of the nanoparticle samples were obtained using a FEI Tecnai F12 microscope operating at 120 keV. At least 100 particles were analyzed per sample to obtain a representative size distribution. High-resolution TEM (HRTEM) was done using a FEI Tecnai F20 microscope operating at 200 keV.

X-ray Diffraction

XRD (X-ray diffraction) spectra were collected using a Bruker General Area Detector Diffraction System (GADDS). Average grain sizes within the nanoparticle samples were determined from the XRD spectra using the Scherrer equation. The correction for instrumental broadening was conducted using the standard Al_2O_3 sample.

All the structural analyses of roxbyite phase in our paper are based on the crystal structure of roxbyite reported in the Canadian Mineral database structure for $Cu_{1.81}S$[13]. Since this latest roxbyite crystal structural details are updated from the one reported in JCPDS 23-0958, the diffraction plane indices in JCPDS 23-0958 (**Fig. 3**) are slightly different from the actual lattice planes discussed in our paper.

X-ray Absorption Spectroscopy

Copper and zinc K-edge x-ray absorption near edge structure (XANES) measurements were carried out at the bending magnet-based F3 beamline of the Cornell High Energy Synchrotron Source (CHESS) at Cornell University, Ithaca, NY. CHESS is a 5.3 GeV light source which operates in top-up mode (positrons) at a ring current of 200 mA. A silicon (220) double-crystal monochromator (DCM) with an energy resolution ($\frac{\Delta E}{E}$) of ~10^{-4} was used to scan x-ray energy across the copper and zinc K-edges. Uniform thin-film nanoparticle samples were prepared by dispersing the nanoparticles in a small volume of toluene and drop casting the nanoparticles onto Kapton tape. Cu_2S (low chalcocite) and CuS reference standards were prepared by dilution with boron nitride powder (100/1, w/w) and subsequent mixing and grinding with a mortar and pestle, the powders were then pressed into pellets. The Cu K-edge XANES of Cu_2S and CuS reference standards were measured at the bending magnet-based C1 beamline of CHESS using a silicon (111) DCM. The detection mode at both F3 and C1 was fluorescent x-ray yield recorded using a Hitachi 4-element silicon vortex detector with an XIA DXP XMAP processor. The detector count rate was kept below 140,000 counts to insure a linear dead-time response. All spectra were normalized to dead-time corrected I_0, measured using an ion chamber upstream of the sample filled with 100% N_2. Copper and zinc reference foil standards used for energy calibration were measured in transmission mode downstream of the sample between two ion chambers filled with 100% N_2. All XANES data were calibrated and normalized using the Demeter Athena XAS software package.[3] Linear combination fitting of XANES data was also performed in Athena.

Scanning Transmission Electron Microscopy

High-angle annular dark-field (HAADF) and electron energy loss spectroscopic (EELS) data were acquired on a 5th-order aberration-corrected scanning transmission electron microscope (Nion UltraSTEM) operated at 100 kV with a probe forming semi-angle of roughly 30 mrad and a collection semi-angle around 80-240 mrad and 0-60 mrad for HAADF and EELS respectively. A Gatan Enfina spectrometer was mounted above (beyond) the collection optics of the microscope for simultaneous HAADF and EELS acquisition. Resolution just below ~1 Angstrom is roughly the information transfer limit for this microscope optimally operating under these conditions.

Continuum model

The force balance equation in any continuum is given by

$$\vec{\nabla} \cdot \boldsymbol{\sigma} + \vec{f} = 0$$

where σ is the cauchy stress tensor and $\vec{f}$ is the body force. Assuming a linear model, the stress tensor can be written as,

$$\sigma_{ij} = C_{ijkl}\epsilon_{kl}$$

where C_{ijkl} is the stiffness tensor and ϵ_{kl} is the strain tensor which under small displacement assumption can be written as

$$\epsilon_{ij} = \frac{1}{2}(u_{i,j} + u_{j,i})$$

where u_{ij} is the derivative along the direction *j* of the component *i* of displacement $\vec{u}$.

Assuming the material to be isotropic, the stiffness tensor can be written as,

$$C_{ijkl} = \lambda\delta_{ij}\delta_{kl} + \mu(\delta_{ik}\delta_{jl} + \delta_{il}\delta_{jk})$$

where λ and μ are the Lame parameters and δ_{ij} is the Kronecker delta function.

The above equations were solved for the spherical nanoparticle using the Finite Element Method (FEM) with the values of Lame parameters obtained from the DFT calculations.

The elastic energy is given by

$$\frac{1}{2}\int_V \sigma_{ij}\epsilon_{ij}dV$$

Density-functional calculation Method

Density-functional calculations were performed with the Vienna Ab-initio Software Package (VASP)[4-7] using the PBE exchange-correlation functional[8] and the projector augmented wave method.[9, 10] The Brillouin zone integration was performed using a Monkhorst and Pack *k*-point mesh.[11] 3×3×3 *k*-point meshes were employed for structural relaxations and nudged-elastic band (NEB) calculations[12] of the 180-atoms roxbyite structure, 144-atoms low chalcocite structure and the CdS/ZnS structures. The kinetic energy cutoff for the plane wave basis was set to 400 eV and the corresponding cutoff energies for the augmentation functions were set to 650 eV for all our calculations. The POSCAR file for roxbyite was

created from the Canadian Mineral database structure for $Cu_{1.81}S$[13] whereas the Materials Project Website[14] was used to get all other POSCAR files. Band gap and dielectric constant calculations were performed on elongated and compressed lattices to study how these properties vary with strain.

X-ray Absorption Absorption Near Edge Fine Structure (XANES)[15]

XANES describes the modulation of the linear X-ray absorption coefficient, μ(*E*), just above the absorption edge of an element, in this case the Cu or Zn, by neighboring atoms. When a photon strikes a material with an energy greater than the excitation energy of a core level electron (E_0) there is a sharp rise (edge) in the absorption coefficient, μ(*E*), this "edge" arises from dipole allowed transitions ($\Delta l \pm 1$, where l is angular momentum) of core level electrons into previously unoccupied electronic states[16]. In the XANES region (from 0 to ~50 eV above the edge) the kinetic energy of the outgoing photoelectron is low, and thus, multiple scattering dominates (for a more rigorous discussion of XANES and multiple scattering see Supporting Information) which adds a fine structure component to the smooth, step-like, absorption profile (known as the atomic absorption coefficient, $\mu_0(E)$) which would be observed from a lone absorbing atom. Therefore, XANES can be thought of as a chemical fingerprint, containing information about the oxidation state (position of the excitation threshold, E_0) and the local chemical environment (number of neighboring atoms and local coordination geometry) of the absorbing atom (in this case either Cu or Zn). Thus, Cu (Zn) K-edge XANES directly probe the oxidation state and local chemical environment of the Cu (Zn) absorber *via* 1s → np (n ≥ 4) dipole allowed transitions.

In the XANES region the incident X-ray photon energy is equal to or just above (~10's of eV) the absorption threshold E_0 resulting in transitions of the core-level electron into previously bound and quasi-bond states. In a multi-atom system there are scattering contributions to the absorption coefficient μ from all the neighbouring atoms resulting in multiple scattering pathways. The total absorption coefficient μ can be written as a function of energy as

$$\mu(E) = \mu_0 \left[1 + \sum\nolimits_{n\geq 2} \chi_n(E)\right] \qquad (1)$$

where μ_0 is the atomic absorption coefficient, n is the number of atoms, and $\chi_n(E)$ contains contributions to the absorption coefficient from all scattering pathways of $n - 1$ neighbouring atoms. Thus there is a strong effect on the amplitude and spectral shape of the XANES spectrum by the local symmetry, crystal structure, and type of the absorbing atoms.

The absorption coefficient, $\mu(E)$, is in theory proportional to the probability that an X-ray photon will be absorbed by an electron in the absorbing atom producing a transition between initial and final quantum states as described by Fermi's Golden Rule

$$\mu(E) \approx \left|\langle\psi_i|H|\psi_f\rangle\right|^2; H = (\hat{\varepsilon}\cdot\vec{r})e^{\left(i(\hat{k}\cdot\vec{r})\right)} \quad (2)$$

where ψ_i is the initial state function which describes a core-level electron, X-ray photon, and no photoelectron; ψ_f is the final state function which describes a photoelectron, *core-hole*, and no X-ray; and *H* is the interaction Hamiltonian between the electromagnetic field of the X-ray and the electron. The Hamiltonian expression includes the electric field vector of the X-ray ε, the forward scattering vector *k*, and the electron coordinate vector *r*. If we further expand the Hamiltonian we get

$$H = (\hat{\varepsilon}\cdot\vec{r}) + (\hat{\varepsilon}\cdot\vec{r})\left(\hat{k}\cdot\vec{r}\right) + \cdots \quad (3)$$

XANES is dominated by the first term in Equation 2-10 which is the dipole component, giving rise to transitions of core-level electrons from 1s to p final states (*K*-edge) and 2p to s + d final states ($L_{3,2}$-edges), etc. which follow the dipole selection rule ($\Delta l = \pm 1$ and $\Delta j = 0$). Although the quadrupole component (the second term of Equation 2-10) is several orders of magnitude weaker it is highly sensitive to metal d-electron–ligand hybridization and gives a strong contribution to the *K*-edge XANES of transition metals which are observed as weak pre-edge features before the main absorption edge[17, 18].

An alternative description of XANES is given by the band structure theory approach described by Muller and Wilkins[19], where the X-ray energy dependence of the absorption coefficient μ can be described as

$$\mu(E) = \frac{4\pi^2\alpha}{\Omega/v}F(E) \quad (4)$$

where α is the inverse fine structure constant ($\alpha^{-1} = 137.036$), Ω is the primitive cell volume, *v* is the number of atoms that contribute to the primitive cell, and *F*(*E*) is the spectral distribution of the oscillator strength. *F*(*E*) contains contributions from both atomic and solid state terms. The observed magnitude and shape of the XANES spectrum is determined by the atomic transition of a core-level electron and fine structure in the spectrum is determined by the solid state term which is proportional to the projected density of states.

LC(Linear combination)-XANES Fitting

Linear combination XANES (LC-XANES) fitting is a common method for determining phase fraction from XAS, and has been used to study mechanisms of gold bioaccumulation[20], iron-monosulfide

oxidation[21], secondary phases in kesterite Cu_2ZnSnS_4 thin films[22], electrochemical delithiation of $LiFePO_4$[23], and (de)lithiation mechanisms in Li/SeS_x (x = 0–7)[24].

In order to quantify the $Cu_{1.81}S$ and Cu_2S contributions to the copper K-edge XANES of the heterostructure NCs, we fit the absorption coefficient $\mu(E)$ with a linear combination of $Cu_{1.81}S$ (roxbyite) and Cu_2S (djurleite / low chalcocite) reference spectra according to (5),

$$\mu(E) = a_\mu \cdot \mu(E)_{Cu_{1.81}S} + b_\mu \cdot \mu(E)_{Cu_2S} \quad (5)$$

where E is the X-ray excitation energy and a_μ and b_μ are the weighting factors of $Cu_{1.81}S$ and Cu_2S, respectively. Fitting of the absorption coefficient $\mu(E)$ of the heterostructured NCs was also attempted using a linear combination of $Cu_{1.81}S$, Cu_2S (djurleite / low chalcocite), and CuS reference spectra; however, it was determined that there are no CuS contributions in the near edge region. The position of E_0 for the heterostructured NC samples, the $Cu_{1.81}S$ roxbyite NC starting materials, and the Cu_2S bulk sample was ~8980 eV, which is consistent with copper in the 1+ oxidation state (E_0 for Cu metal is 8979 eV). The fitting results are shown in **Table S2**. LC-XANES fitting of NC sample with t = 20 nm is shown in **Fig. S7**.

Scanning Transmission Electron Microscopy

The background EELS spectrum was modeled using a linear combination of power laws and a conservative local background average ranging from 1.5 to 2 pixels FWHM (smaller than the probe width). This provided a marginal improvement over traditional power law background modeling. These techniques were implemented using the open-source Cornell Spectrum Imager software and are described in more detail by P. Cueva et al.[25]

The sulfur EELS signal was obtained by integration over the $L_{2,3}$ core loss edge after background subtraction. The copper and zinc $L_{2,3}$ core loss edges start at 931 and 1020 eV respectively, with the Zn signal resting atop part of the Cu edge. To decompose the convoluted spectrum, reference spectrum obtained from an average of spectra in Cu or Zn regions were obtained and non-negative least square regression was performed.[26] Better quantification of the Zn and Cu concentrations in the intermediate stage NC—where the Cu SNR was higher—was obtained (**Fig. S21a,b**) through multivariate curve resolution (MCR) methods.[27-30] MCR was performed over 20 iterations to extract the spectral components—**Fig. S21d** shows typical Cu and Zn MCR components.

References

1. Li, W.; Shavel, A.; Guzman, R.; Rubio-Garcia, J.; Flox, C.; Fan, J.; Cadavid, D.; Ibanez, M.; Arbiol, J.; Morante, J. R.; Cabot, A. *Chem. Commun.* **2011,** 47, (37), 10332-10334.
2. Xie, Y.; Riedinger, A.; Prato, M.; Casu, A.; Genovese, A.; Guardia, P.; Sottini, S.; Sangregorio, C.; Miszta, K.; Ghosh, S.; Pellegrino, T.; Manna, L. *J. Am. Chem. Soc.* **2013,** 135, (46), 17630-17637.
3. Ravel, B.; Newville, M. *J. Synchrotron Radiat.* **2005,** 12, (4), 537-541.
4. Kresse, G.; Hafner, J. *Phys. Rev. B* **1993,** 47, (1), 558.
5. Kresse, G.; Hafner, J. *Phys. Rev. B* **1994,** 49, (20), 14251.
6. Kresse, G.; Furthmüller, J. *Comput. Mater. Sci.* **1996,** 6, (1), 15-50.
7. Kresse, G.; Furthmüller, J. *Phys. Rev. B* **1996,** 54, (16), 11169.
8. Perdew, J. P.; Burke, K.; Ernzerhof, M. *Phys. Rev. Lett.* **1996,** 77, (18), 3865.
9. Blöchl, P. E. *Phys. Rev. B* **1994,** 50, (24), 17953.
10. Kresse, G.; Joubert, D. *Phys. Rev. B* **1999,** 59, (3), 1758.
11. Monkhorst, H. J.; Pack, J. D. *Phys. Rev. B* **1976,** 13, (12), 5188.
12. Jónsson, H.; Mills, G.; Jacobsen, K. W., Nudged elastic band method for finding minimum energy paths of transition. In *Classical and quantum dynamics in condensed phase simulations*, World Scientific: 1998; pp 385-404.
13. Mumme, W. G.; Gable, R. W.; Petříček, V. *Can. Mineral.* **2012,** 50, (2), 423-430.
14. Ong, S. P.; Jain, A.; Hautier, G.; Kocher, M.; Cholia, S.; Gunter, D.; Bailey, D.; Skinner, D.; Persson, K.; Ceder, G. *https://materialsproject.org*.
15. Ward, M. J. X-ray Absorption Fine Structure and X-ray Excited Optical Luminescence Studies of Gallium Nitride-Zinc Oxide Solid Solution Nanostructures. The University of Western Ontario, 2013.
16. Ward, M. J.; Rupar, P. A.; Murphy, M. W.; Yiu, Y.-M.; Baines, K. M.; Sham, T. *Chem. Commun.* **2010,** 46, (37), 7016-7018.
17. De Groot, F. *Chem. Rev.* **2001,** 101, (6), 1779-1808.
18. De Groot, F.; Kotani, A., *Core level spectroscopy of solids*. CRC press: 2008.
19. Müller, J. E.; Wilkins, J. W. *Phys. Rev. B* **1984,** 29, (8), 4331.
20. Lengke, M. F.; Ravel, B.; Fleet, M. E.; Wanger, G.; Gordon, R. A.; Southam, G. *Environ. Sci. Technol.* **2006,** 40, (20), 6304-6309.
21. Burton, E. D.; Bush, R. T.; Sullivan, L. A.; Hocking, R. K.; Mitchell, D. R. G.; Johnston, S. G.; Fitzpatrick, R. W.; Raven, M.; McClure, S.; Jang, L. Y. *Environ. Sci. Technol.* **2009,** 43, (9), 3128-3134.
22. Just, J.; Lützenkirchen-Hecht, D.; Frahm, R.; Schorr, S.; Unold, T. *Appl. Phys. Lett.* **2011,** 99, (26), -.
23. Yu, X.; Wang, Q.; Zhou, Y.; Li, H.; Yang, X.-Q.; Nam, K.-W.; Ehrlich, S. N.; Khalid, S.; Meng, Y. S. *Chem. Commun.* **2012,** 48, (94), 11537-11539.
24. Cui, Y.; Abouimrane, A.; Lu, J.; Bolin, T.; Ren, Y.; Weng, W.; Sun, C.; Maroni, V. A.; Heald, S. M.; Amine, K. *J. Am. Chem. Soc.* **2013,** 135, (21), 8047-8056.
25. Cueva, P.; Hovden, R.; Mundy, J. A.; Xin, H. L.; Muller, D. A. *Microsc. Microanal.* **2012,** 18, (04), 667-675.
26. Bro, R.; De Jong, S. *J. Chemom.* **1997,** 11, (5), 393-401.
27. Sylvestre, E.; Lawton, W.; Maggio, M. *Technometrics* **1974,** 16, (3), 353-368.
28. Tauler, R.; Izquierdo-Ridorsa, A.; Casassas, E. *Chemometr. Intell. Lab.* **1993,** 18, (3), 293-300.
29. Kotula, P. G.; Keenan, M. R. *Microsc. Microanal.* **2006,** 12, (06), 538-544.
30. Kotula, P. G.; Keenan, M. R.; Grant, R. P.; Hlava, P. F. *Microsc. Microanal.* **2004,** 10, (S02), 118-119.